Geophysical Journal International

Geophys. J. Int. (2015) **202,** 1677–1689
GJI Gravity, geodesy and tides

doi: 10.1093/gji/ggv244

The 2012 August 27 M_w7.3 El Salvador earthquake: expression of weak coupling on the Middle America subduction zone

Halldor Geirsson,[1,2] Peter C. LaFemina,[1] Charles DeMets,[3] Douglas Antonio Hernandez,[4] Glen S. Mattioli,[5,6] Robert Rogers,[7] Manuel Rodriguez,[8] Griselda Marroquin[4] and Virginia Tenorio[9]

[1]*Department of Geosciences, The Pennsylvania State University, University Park, PA, USA. E-mail: hgeirsson@psu.edu*
[2]*European Center for Geodynamics and Seismology, Walferdange, Luxembourg*
[3]*Department of Geoscience, University of Wisconsin-Madison, Madison, WI, USA*
[4]*Servicio Nacional de Estudios Territoriales, San Salvador, El Salvador*
[5]*UNAVCO, Boulder, CO, United States*
[6]*Department of Earth and Environmental Sciences, University of Texas at Arlington, Arlington, TX, USA*
[7]*Department of Geology, California State University - Stanislaus, Turlock, CA, USA*
[8]*Instituto Hondureno de Ciencias de la Tierra, Universidad Nacional Autonoma de Honduras, Tegucigalpa, Honduras*
[9]*Geophysics Department, Instituto Nicaraguense de Estudios Territoriales, Managua, Nicaragua*

Accepted 2015 June 5. Received 2015 June 4; in original form 2015 February 4

SUMMARY

Subduction zones exhibit variable degrees of interseismic coupling as resolved by inversions of geodetic data and analyses of seismic energy release. The degree to which a plate boundary fault is coupled can have profound effects on its seismogenic behaviour. Here we use GPS measurements to estimate co- and post-seismic deformation from the 2012 August 27, M_w7.3 megathrust earthquake offshore El Salvador, which was a tsunami earthquake. Inversions of estimated coseismic displacements are in agreement with published seismically derived source models, which indicate shallow (<20 km depth) rupture of the plate interface. Measured post-seismic deformation in the first year following the earthquake exceeds the coseismic deformation. Our analysis indicates that the post-seismic deformation is dominated by afterslip, as opposed to viscous relaxation, and we estimate a post-seismic moment release one to eight times greater than the coseismic moment during the first 500 d, depending on the relative location of coseismic versus post-seismic slip on the plate interface. We suggest that the excessive post-seismic motion is characteristic for the El Salvador–Nicaragua segment of the Central American margin and may be a characteristic of margins hosting tsunami earthquakes.

Key words: Seismic cycle; Transient deformation; Tsunamis; Creep and deformation; Friction.

1 INTRODUCTION

Over the last several decades a broad spectrum of fault behaviours has been imaged through geodetic and seismic studies of the earthquake cycle. At one end of the spectrum, earthquakes represent near-instantaneous high-strain rate events, whereas at the other end of the spectrum episodic slow-slip events and transient afterslip following intermediate to large magnitude earthquakes represent low strain rate events that may occur over weeks to years. Within this spectrum lie 'tsunami earthquakes', which produce unusually large tsunamis compared to their magnitude (Kanamori 1972; Satake & Tanioka 1999; Kanamori 2014). Tsunami earthquakes are distinct from regular earthquakes (that may be tsunami-genic), by their abnormally long rupture duration and depletion of high frequencies in radiated energy. Examples of tsunami earthquakes include the 1992 Nicaragua (Kanamori & Kikuchi 1993) and the 2010 Mentawai earthquakes (Hill *et al.* 2012). An interesting aspect of tsunami earthquakes is that they rupture the shallowest part of the subduction interface (<20 km depth), which has been suggested to be generally unable to accumulate large amounts of strain (e.g. Byrne *et al.* 1988) because of the low strength of subducting sediment. Ruptures associated with tsunami earthquakes may propagate up-dip into or through the sediments (Polet & Kanamori 2000). Sediment-poor subduction zones such as offshore Nicaragua and El Salvador can thus facilitate shallow ruptures. Tsunami earthquakes are rare, but pose significant threats to coastal regions. Therefore, it is important

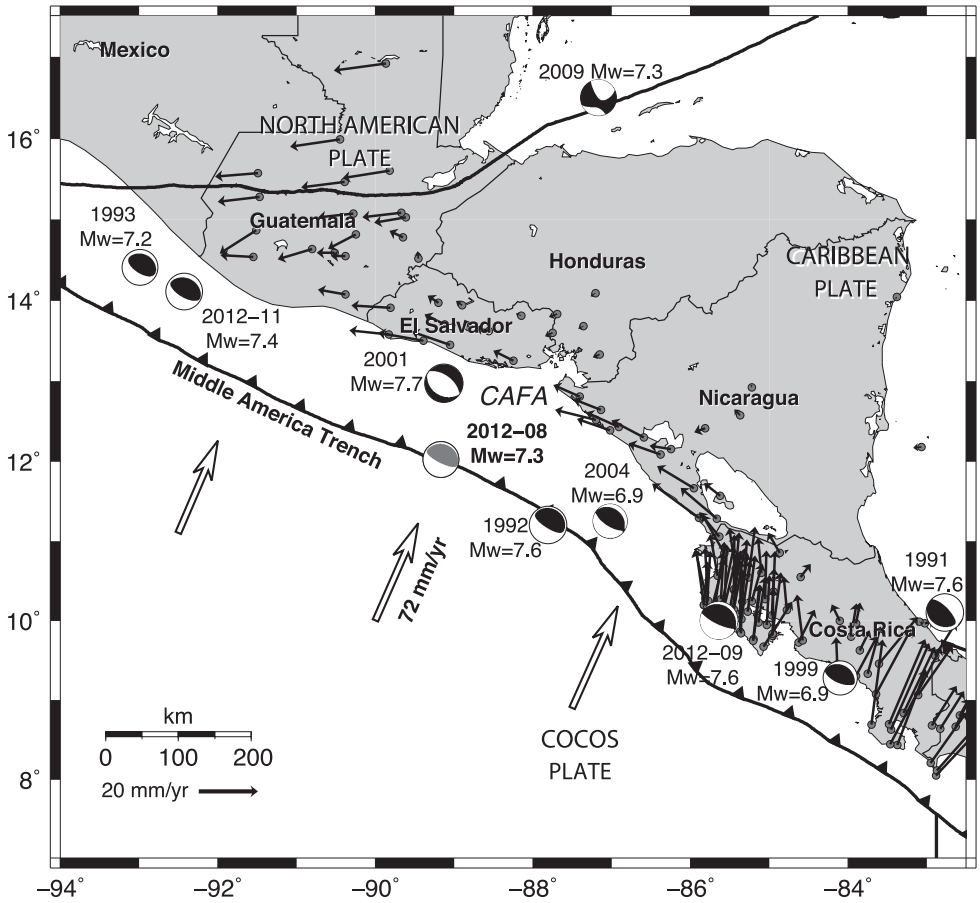

Figure 1. Tectonic setting of Central America. Focal mechanisms and earthquake locations (moment tensor centroids) are from the GCMT project; the focal mechanism for the 2012 August 27, El Salvador earthquake is coloured grey. White vectors show the motion of the Cocos Plate relative to the Caribbean Plate (DeMets *et al.* 2010). Black vectors show interseismic GPS-site velocities relative to the Caribbean Plate (from Kobayashi *et al.* 2014). CAFA, Central American forearc.

to investigate them with available geodetic and seismic observations when possible to improve our understanding of the source processes.

The Middle America Trench (MAT) marks the boundary where the Cocos Plate subducts under the Caribbean Plate at rates ranging from 67 mm yr^{-1} at the latitude of Guatemala to 77 mm yr^{-1} offshore the Nicoya peninsula, Costa Rica (DeMets *et al.* 2010) (Fig. 1). Studies of the subduction zone earthquake cycle here are complicated by the northwest movement of the Central American forearc (CAFA) microplate (i.e. the region between the MAT and the volcanic arc; Fig. 1; Kobayashi *et al.* 2014) relative to the Caribbean Plate, and the distance between the MAT and terrestrial geodetic networks. Estimates of the motion of the CAFA microplate relative to the Caribbean Plate from earthquake slip vectors and GPS data range from 10 to 16 mm yr^{-1} towards the northwest (DeMets 2001; Turner *et al.* 2007; Correa-Mora *et al.* 2009; LaFemina *et al.* 2009; Kobayashi *et al.* 2014). Consequently, the Cocos—CAFA convergence is 76 mm yr^{-1} in a direction N29° offshore El Salvador (Kobayashi *et al.* 2014). That interseismic GPS velocities in El Salvador and Nicaragua do not show a significant trench-normal component of motion relative to the Caribbean Plate (Fig. 1) indicates that Cocos–Caribbean convergence along the subduction interface is dominated by creep [i.e. there is low or no coupling between the plates (Correa-Mora *et al.* 2009; LaFemina *et al.* 2009; Kobayashi *et al.* 2014)]. LaFemina *et al.* (2009), however, indicate that coupling must occur offshore based on the inversion of geodetic data and the occurrence of earthquakes along the margin, but that the coupled region is limited to above 20 km depth (85–150 km from land).

The El Salvadoran segment of the Middle America subduction zone has historically been a seismic gap for megathrust earthquakes (e.g. Dewey *et al.* 2004; Kobayashi *et al.* 2014). Historical accounts of earthquake damage (White *et al.* 2004) and tsunamis (Fernández *et al.* 2004), and instrumental records (Ambraseys & Adams 1996) indicate that the last earthquake to rupture the southern segment of the El Salvadoran subduction zone occurred in 1919 or earlier. The last major earthquake along the margin was the 2001 January 13 M_w7.7 intraslab normal faulting earthquake (Fig. 1; Valleé *et al.* 2003). This event was followed by a M_w6.6 shallow strike-slip event in February 2001 at the CAFA–Caribbean Plate boundary (Bommer *et al.* 2002; Martínez-Díaz *et al.* 2004). In fact, shallow strike slip events along the CAFA–Caribbean Plate boundary have caused much localized damage and are a serious seismic hazard in the region.

In 2012 the Middle American subduction zone was struck by three $M_w \geq 7.3$ megathrust earthquakes (Fig. 1). The first earthquake occurred on 2012 August 27 at 04:37:20 UTC (August 26 at 22:37:20 local time) offshore El Salvador. This earthquake had a magnitude of M_w7.3 and generated a small tsunami with a maximum run-up of approximately 5 m observed on the coasts of El Salvador and western Nicaragua (H. Fritz, private communication, 2012). The earthquake displayed clear seismologic characteristics

of a tsunami earthquake (Ye *et al.* 2013). Nine days later on 2012 September 5 at 14:42:08 UTC, a M_w7.6 earthquake occurred under the Nicoya Peninsula, Costa Rica (Protti *et al.* 2013). Finally, on 2012 November 7, at 16:35:50 UTC, a M_w7.4 earthquake occurred offshore southwestern Guatemala (Ye *et al.* 2013; Ellis *et al.* 2015). The 2012 August 27, El Salvador earthquake is a major event for this part of the plate boundary despite its small magnitude in a global context and gives insights into regional fault behaviour and tsunami earthquakes. In this study, we use global positioning system (GPS) data and earthquake locations to investigate the co- and post-seismic deformation associated with this event and discuss our results in terms of the strain accumulation and slip characteristics of the weakly coupled subduction zone offshore El Salvador and Nicaragua.

2 DATA AND ANALYSIS

2.1 GPS data collection and processing

In order to estimate co- and post-seismic deformation due to the 2012 El Salvador earthquake, we use a combination of continuous GPS (cGPS) and episodic GPS (eGPS; also known as 'campaign GPS') data from El Salvador, Guatemala, Honduras, and Nicaragua (see Fig. 2 for site locations). We use cGPS data from five stations in El Salvador, three stations in Guatemala, one station in Honduras and four stations in Nicaragua. There are currently 14 cGPS stations running in Nicaragua; however, ten of those cGPS stations are at Telica volcano (Geirsson *et al.* 2014; Fig. 2) and did not yield significant coseismic offsets for the El Salvador earthquake. We augment the cGPS data observations with eGPS data from El Salvador (four stations), southern Honduras (four stations), and western Nicaragua (one station). The eGPS sites were observed for at least 24 hr during each occupation. Episodic GPS site CHIN (Nicaragua) was occupied continuously from 2012 September 2 onwards. The GPS data were processed with the GIPSY/OASIS II software (Zumberge *et al.* 1997) using the AMBIZAP3 algorithm for ambiguity resolution (Blewitt 2008). Time-series for selected eGPS and cGPS sites are shown in Fig. 3, where we have estimated and removed the pre-seismic average velocity for each site.

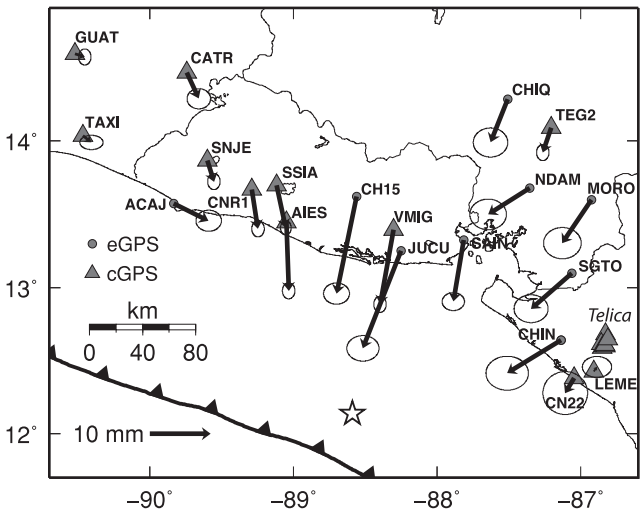

Figure 2. Map of estimated coseismic displacements (black vectors) with 1σ uncertainties at our geodetic GPS network sites. Epicentral location of the 2012 August 27 El Salvador earthquake from USGS-NEIC is shown with a star.

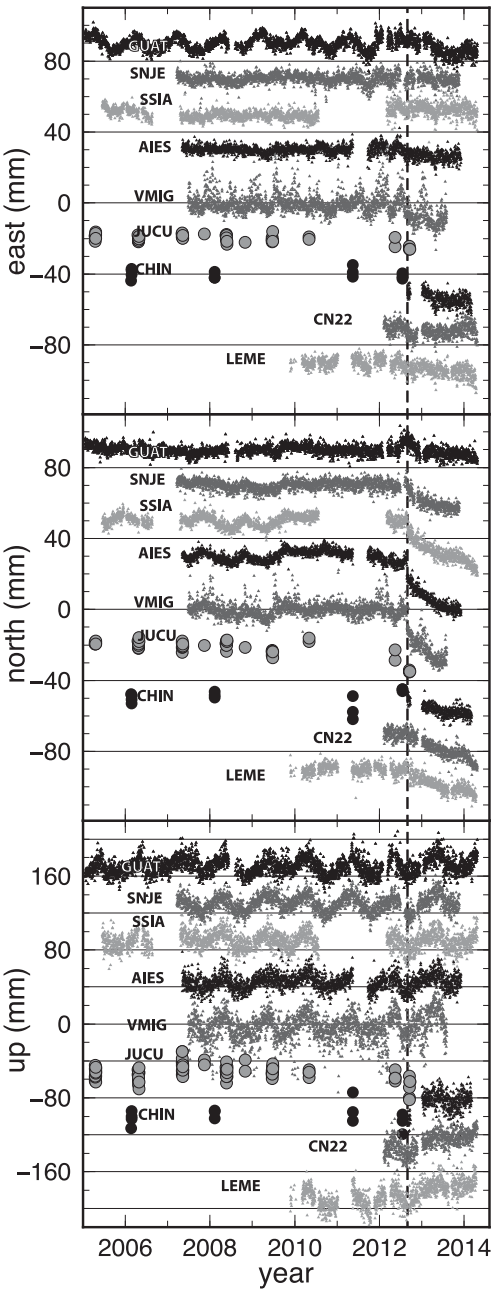

Figure 3. GPS time-series from selected stations in El Salvador and Nicaragua in east, north, and vertical components. See Fig. 2 for site locations. The time of the 2012 El Salvador earthquake is marked with a dashed line. Episodic GPS data are shown with circles while cGPS data are shown with triangles. Each station is detrended using its mean velocity during 2005–2012. Annual signals and data outliers have not been removed, nor has a network filter been applied.

2.2 Coseismic deformation

The coseismic offsets and subsequent post-seismic deformation are most pronounced in the north component of the GPS time-series (Fig. 3). The coseismic offsets were estimated using two different methods, depending on whether the GPS data were collected episodically or continuously. We applied a network filter (Wdowinski *et al.* 1997) to all time-series before the coseismic offset estimation in order to minimize common-mode error. For cGPS site time-series the offsets were estimated by differencing 5-d weighted position

Table 1. Coseismic offsets at GPS stations. Uncertainties are 1σ.

Station	Delay*	Latitude	Longitude	East (mm)	North (mm)	Up (mm)
ACAJ	179	13.58	−89.83	5.8 ± 1.4	−2.9 ± 1.2	−8.9 ± 5.3
AIES	c	13.45	−89.05	0.4 ± 0.7	−11.3 ± 0.9	−3.4 ± 3.0
CATR	c	14.46	−89.74	2.0 ± 1.3	−4.3 ± 1.1	3.9 ± 4.8
CH15	25	13.62	−88.56	−3.3 ± 1.4	−16.0 ± 1.2	−17.4 ± 5.4
CHIN	6	12.64	−87.14	−8.9 ± 2.4	−5.4 ± 1.9	−8.2 ± 6.3
CHIQ	293	14.28	−87.51	−2.8 ± 1.9	−7.1 ± 1.6	−3.8 ± 7.2
CN22	c	12.38	−87.04	−1.5 ± 2.5	−2.5 ± 2.4	−1.1 ± 7.8
CNR1	c	13.67	−89.29	1.0 ± 0.7	−6.5 ± 0.9	1.3 ± 3.1
GUAT	c	14.59	−90.52	1.6 ± 0.7	−0.5 ± 0.9	0.7 ± 1.5
JUCU	21	13.25	−88.25	−6.3 ± 1.8	−16.1 ± 1.4	−23.1 ± 6.5
LEME	c	12.43	−86.91	0.5 ± 1.6	0.7 ± 1.2	1.6 ± 1.9
MANA	c	12.15	−86.25	−0.1 ± 1.6	−1.7 ± 1.9	2.4 ± 8.2
MORO	289	13.60	−86.92	−4.8 ± 2.1	−7.1 ± 1.8	16.7 ± 7.8
NDAM	285	13.68	−87.36	−6.8 ± 2.0	−4.3 ± 1.7	−10.1 ± 7.5
SAIN	165	13.32	−87.82	−1.7 ± 1.2	−10.1 ± 1.0	5.3 ± 4.7
SGTO	286	13.10	−87.06	−6.7 ± 1.9	−5.9 ± 1.6	7.2 ± 7.1
SNJE	c	13.87	−89.60	1.1 ± 0.7	−3.5 ± 0.9	3.1 ± 2.3
SSIA	c	13.70	−89.12	1.5 ± 0.6	−7.0 ± 0.8	−2.4 ± 1.8
TAXI	c	14.03	−90.47	1.4 ± 1.3	−1.1 ± 0.8	0.3 ± 4.5
TEG2	c	14.09	−87.21	−1.4 ± 0.7	−4.1 ± 0.9	−1.5 ± 1.5
VMIG	c	13.40	−88.30	−2.2 ± 0.7	−12.3 ± 0.9	−0.5 ± 2.5

Notes. *Time in days that passed since the earthquake until the first (daily) measurement. 'c' stands for a continuous GPS site and indicates no delay.

averages before and after the earthquake. For the eGPS time-series, we corrected for coseismic deformation from the 2009 May 28, M_w7.3 Swan Islands fault earthquake (Graham *et al.* 2012), detrended the time-series using data up until the earthquake (from 2005.0 to 2012.65), and then estimated the coseismic offsets directly. The 9-d interval between the 2012 August 27, El Salvador and 2012 September 5, Nicoya earthquakes allows us to estimate coseismic offsets for the El Salvador earthquake independent of Nicoya earthquake coseismic offsets at the cGPS stations. Episodic GPS site CHIN was also running at the time of the 2012 September 5, Nicoya earthquake and showed insignificant displacements for that earthquake. This observation is in agreement with predicted displacements calculated from the USGS finite-fault model of Hayes (2012) for the 2012 September 5, Nicoya earthquake. The pattern of coseismic displacements for the 2012 August 27 earthquake points towards the USGS NEIC epicentre (Fig. 2; Table 1), as is typical for offshore subduction thrust earthquakes recorded by onshore geodetic networks. The maximum observed coseismic displacement is 17 mm at eGPS site JUCU in eastern El Salvador.

The coseismic offset estimates for the eGPS sites, and to a lesser degree those for the cGPS sites, are affected by post-seismic deformation following the 2012 earthquake (Fig. 3), because the measurements were not made instantaneously after the earthquake (Table 1). This causes a bias in the coseismic estimates because some of the post-seismic deformation will be incorporated into the coseismic displacement estimates. For example, Hill *et al.* (2012) estimated from comparison of high-rate and 24-hr processing of cGPS data for the M_w7.8 2010 Mentawai earthquake that ∼30 per cent of the coseismic offsets based on the 24-hr solutions were in fact post-seismic deformation. We processed 30-s data in kinematic mode for cGPS stations in El Salvador (AIES, SSIA, and VMIG) to examine the coseismic offsets and to see if rapid post-seismic deformation could be detected. The kinematic time-series are of course much noisier than the daily solutions; nevertheless, they show coseismic offsets on the order of 1 cm southward (Fig. S1), verifying that our offset estimates from daily processing for the cGPS sites (Table 1) are indeed of the coseismic deformation. This is, however, not the case for the eGPS measurements, where the post-seismic contamination depends on the time between the earthquake and the measurement (Table 1) and the extent and amplitude of the post-seismic deformation (see next section).

2.3 Post-seismic deformation

Considerable post-seismic deformation following the 2012 August 27 earthquake is observed at the cGPS stations in El Salvador (Figs 3 and 4). For example, station AIES moved ∼16 mm southwards (N190°) during the first year following the earthquake, compared to 11 mm southwards for the coseismic offset. There are seasonal signals in the horizontal and vertical components of the cGPS position time-series (Fig. 3), which can affect our interpretation and estimation of the post-seismic signal. Because of the seasonal signals we estimate linear, annual, and semi-annual parameters for each of the cGPS time-series components from pre-seismic data (2005 or later, depending on data availability) and apply these to the entire time-series to remove steady-state (i.e. tectonic motion) and annually cyclic movements. We did not apply network filtering to the data here because we can estimate the seasonal signals independently for the cGPS sites. For episodic site CHIN, which was operated in continuous mode following the El Salvador earthquake, and sites CN22 and TEG2, which have time-series too short before the El Salvador earthquake to allow for meaningful estimates of seasonal components, we only applied a linear correction based on pre-seismic data. The resulting time-series for the north component of the cGPS sites (Fig. 4b) show a generally decaying trend of post-seismic motion.

We estimated the cumulative post-seismic offsets for cGPS station time-series in the east and north components every 100 d following the time of the El Salvador earthquake (Table S1 and Fig. 4). We did not observe any significant post-seismic deformation in the vertical component. To estimate the post-seismic deformation, we first removed the linear and seasonal signals estimated from pre-seismic data, as described above. To avoid including coseismic deformation from the Nicoya earthquake in our post-seismic

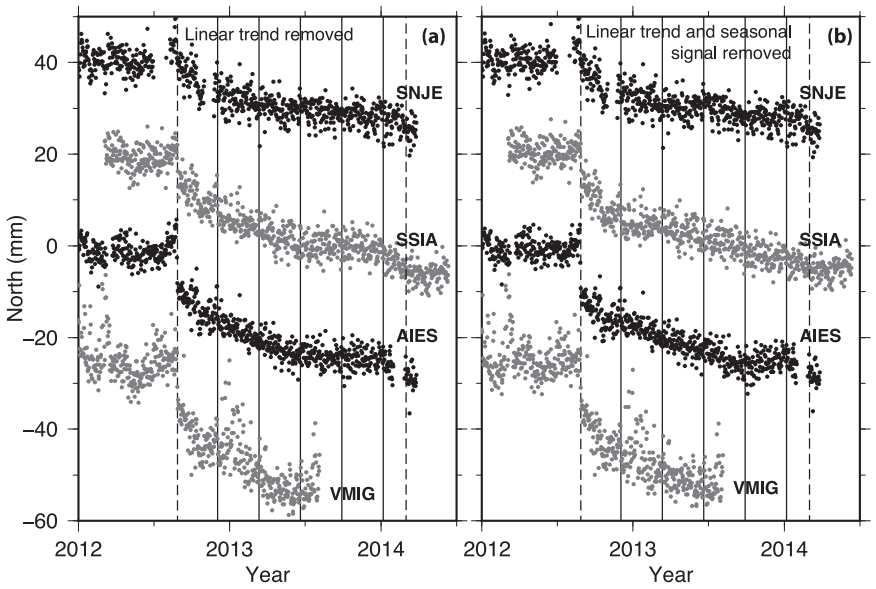

Figure 4. GPS time-series for the north component of cGPS stations in El Salvador. (a) Linear trend estimated from the time period 2005.0–2012.6 has been removed; (b) Linear trend and annual and semi-annual signals estimated from the time period 2005.0–2012.6 have been removed. The dashed vertical lines mark the time of the 2012 August 27 El Salvador, and the 2014 March 2 Cosiguina earthquakes. Solid vertical lines at 100, 200, 300, 400 and 500 d after the earthquake, show times used for estimating post-seismic deformation.

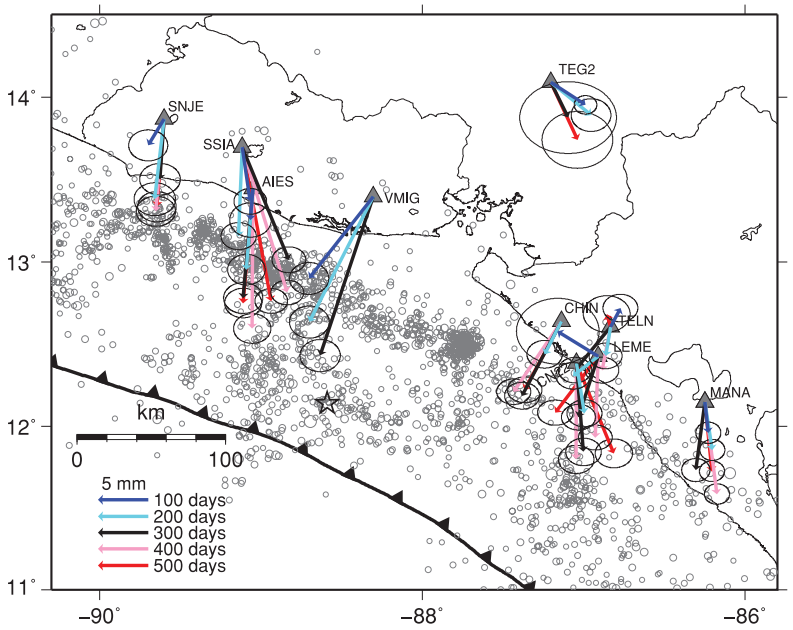

Figure 5. Cumulative post-seismic displacements at 100, 200, 300, 400 and 500 d after the 2012 El Salvador earthquake. Grey circles show earthquake locations near the subduction zone from the El Salvador and Nicaraguan seismic networks from 2012 August 27 to 2014 June 30. Epicentral location of the 2012 August 27 El Salvador earthquake from USGS–NEIC is shown with a star.

estimates, we refer the post-seismic offsets to a 10-d position average after the Costa Rica earthquake for sites LEME, CN22 and TELN.

The cGPS sites in El Salvador record post-seismic motion approximately towards the epicentral region (Fig. 5). The similarity in the azimuths of the post-seismic and coseismic displacements (Fig. 2), suggests that the co- and post-seismic slip distributions affect similar areas of the subduction interface. Sites in Nicaragua show trenchward displacements that may indicate some post-seismic slip occurs directly offshore Nicaragua. The southward motion of site MANA in Nicaragua, towards the Nicoya earthquake epicentre, indicates that its post-seismic deformation is dominated by the Nicoya event (Fig. 5). The southwestward azimuth of motion of sites CHIN, LEME and TELN (Fig. 5) demonstrates that motion of those sites is dominated by post-seismic deformation from the El Salvador earthquake rather than the Nicoya earthquake because otherwise the deformation would be more south- or southeastward towards the Nicoya epicentre (e.g. MANA). Sites TEG2 and CN22 trend to the south or southeast; however, both TEG2 and CN22 have short (1.5 and 0.5 yr, respectively) time-series for estimation of the pre-seismic velocities, which can degrade the estimation of the post-seismic deformation.

3 MODELLING AND RESULTS

3.1 Coseismic deformation

We model the observed coseismic deformation in terms of slip on the Middle America subduction zone megathrust. We use the TDEFNODE software (McCaffrey 2009) to invert the geodetically estimated coseismic offsets for displacement on the megathrust. We adapt the plate interface geometry from the SLAB1.0 subduction zone plate interface model (Hayes *et al.* 2012; Fig. S2a) and represent the plate interface by a grid consisting of a maximum of 33 along-strike and 18 downdip nodes. The numbers of along-strike and downdip nodes that are used in the data inversions vary between the different model types we tested (see below). Displacements are calculated assuming a uniform, elastic half-space with a shear modulus of 40 GPa.

TDEFNODE offers several different approaches to parametrize the distribution of coseismic slip. In order to explore the range of slip distributions that may fit our GPS displacements, we tested the following five different models of slip distribution: (i) Slip at each node [smoothed; grid consisting of 17 along-strike by 18 downdip nodes; each downdip pair of nodes is constrained to have the same slip (Figs 6a and b)]; (ii) Slip at each node (smoothed; grid consisting of 17 along-strike by four downdip nodes). In this model, we forced slip to be near the trench (i.e. the uppermost 10 km of the subduction zone) by eliminating all but the top four downdip nodes (Fig. 6c); (iii) Slip modelled as a Gaussian function of depth, using a grid consisting of 25 along-strike and 18 downdip nodes (Fig. 6d). Here we solved for the centre, spread, and slip amplitude of the Gaussian function along each set of downdip nodes; (iv) Slip modelled as a single rectangular patch with uniform slip and gradual tapering (Fig. 6e). Here we solve for the centre location, slip amplitude, and along-strike and downdip width of the rectangular patch; (v) Slip modelled as a single 2-D Gaussian distribution on the slab interface (Fig. 6f). Here we solve for the centre location, amplitude, and along-strike and along-dip spread of the distribution. For all of the model types the rake was constrained to the Cocos–Caribbean Plate convergence azimuth, which is approximately perpendicular to the strike of the trench offshore El Salvador. For the parameter optimization we employ sequential simulated annealing and grid search, minimizing the sum of weighted residuals, $\chi^2 = \Sigma[(O - E)/\sigma]^2$, where O are the observations with uncertainties σ, and E are the model predictions. Initial slip was assumed to be 0.0 m over the entire fault before each inversion.

We tested the resolution that our network and fault geometry offers for coseismic slip on the plate interface via a series of checkerboard tests using model (i) from above (Fig. S3). While the overall slip-pattern is fairly well recovered (i.e. slip versus no slip) for rectangular patches larger than approximately 100 km by 100 km, the slip amplitudes are not well recovered. This is a well-known trade-off in geodesy, whereby small high-slip patches generate similar deformation as large, low-slip patches centred on the same location. Although the slip-patch dimensions and magnitudes are uncertain, the geodetic moment is typically robustly determined.

We find that all five models tested can fit the coseismic deformation reasonably well. All five models indicate that the greatest slip coincides with the location of the seismically determined epicentres and that most of the slip occurred at depths shallower than ~25 km (Figs 6 and S4). The model residuals are largest in the eastern area of our network, but do not show a coherent pattern (Fig. 6). The coseismic displacements are equally well fit by either large slip (maximum slip greater than 4 m) over a small area (Figs 6b and c) or low slip (maximum slip as low as ~0.2 m) over a larger area (e.g. Fig. 6d). Models that solve for details of the slip distribution, that is slip modelled at each node (model i), or slip modelled as Gaussian functions along each downdip profile (model iii), fit the data similarly well with $\chi^2 = 88$ and 90, respectively. Model (iii) predicts somewhat deeper slip than model (i) (Fig. 6d). Models with simpler representations of slip, that is, a single rectangular slip patch (model iv) or a single 2-D Gaussian slip distribution (model v) fit the data worse than models (i)–(iii) ($\chi^2 \approx 115$ vs. $\chi^2 \approx 88$), but of course have many fewer parameters. Our preferred best-fitting model has a smoothed slip distribution (model i) with maximum slip located between 8 and 15 km depth, coinciding with the seismically determined epicentres (Fig. 6a; Tables S2–S8).

As mentioned above, we cannot fully separate the co- and post-seismic deformation at the eGPS sites. The most poorly fit coseismic offset for any of the models is that for eGPS site CH15 (Figs 4 and 6). CH15 was occupied 25 d after the earthquake and may thus include 25 per cent or more of post-seismic deformation by comparison with nearby cGPS sites (Fig. 4). We reran a subset of our models excluding site CH15 and found that while the χ^2 value drops from 88 to 64 (model i), the overall slip distribution or fit to other sites did not change significantly (Figs 6g and h).

The geodetically estimated moments for all models tested range from 7.7×10^{19} to 1.4×10^{20} Nm (M_w7.2–M_w7.4) (Fig. 6), even when the slip is constrained to be above ~10 km depth (model ii; Fig. 6c). The predicted displacements from the seismologically determined slip distribution of Ye *et al.* (2013) (Fig. S5) fit the coseismic displacements reasonably well ($\chi^2 = 132$). The seismic model of Ye *et al.* (2013) has a maximum slip of ~1 m between 5 and 15 km depth, and a moment of 9.6×10^{19} Nm (M_w7.3), in agreement with our inversion of geodetic data.

3.2 Post-seismic deformation

Post-seismic deformation is commonly explained by afterslip on the fault that ruptured during the earthquake, viscoelastic relaxation in the lower crust and upper mantle, poroelastic rebound in the upper crust, or a combination thereof. In general it is difficult to distinguish between these different deformation mechanisms. Here we consider modelling the observed post-seismic deformation signal as either afterslip or viscoelastic relaxation.

Viscoelastic relaxation depends predominantly on the viscosity structure of the crust and mantle, as well as the magnitude and location of the coseismic moment release. Because the structure and rheology of the Central American margin is not well known, we test a range of rheological models. We assume the same range of crustal models as Norabuena *et al.* (2004) for offshore Nicaragua: a 16 km thick elastic upper crust (30 GPa shear modulus), a Maxwell-viscoelastic lower crust between 16 and 30 km, and a Maxwell viscoelastic half-space (upper mantle) below 30 km depth. We test viscosities between 1×10^{17} and 1×10^{20} Pa s for each of the viscoelastic layers in order to estimate what viscosities would be needed to explain the post-seismic deformation if the observations are dominantly caused by viscoelastic relaxation. We calculate the viscoelastic response using the program RELAX (Barbot *et al.* 2009; Barbot & Fialko 2010) and use the coseismic slip model of Ye *et al.* (2013) as input. To explain the entire observed post-seismic deformation signal as a viscoelastic response, viscosities of 10^{17} and 10^{17}–10^{18} Pa s are required for the upper mantle and lower crust, respectively (Fig. 7). Norabuena *et al.* (2004) use limited GPS data in Costa Rica following the 1992 Nicaragua earthquake

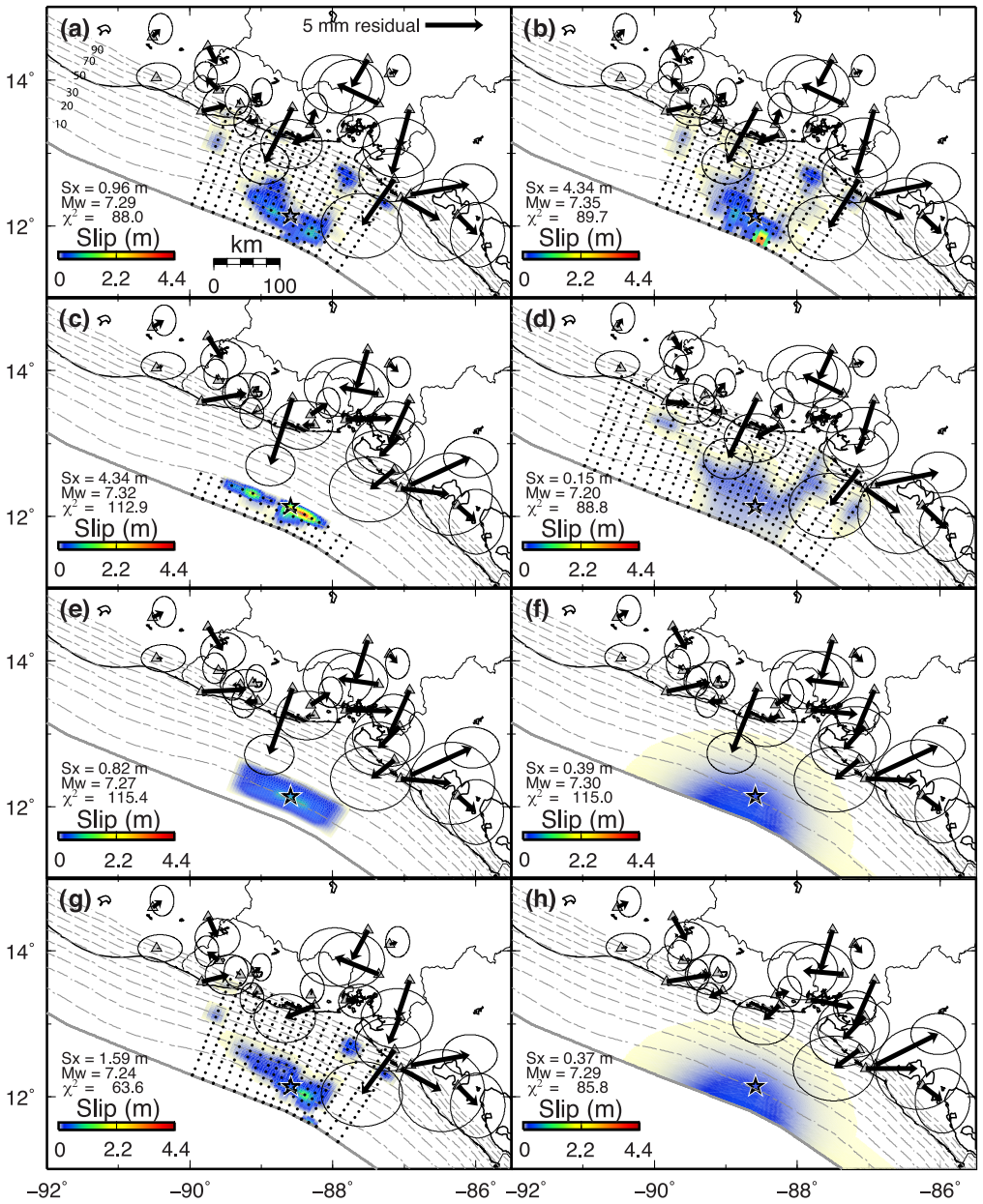

Figure 6. Surface projections of estimated coseismic slip distributions for each of the models tested. See text for further model descriptions. (a) and (b) Two comparably good solutions of model (i), where slip is modelled at independent nodes (black points). (c) Solution of model (ii), where the slip is forced to be near the trench by eliminating downdip nodes. (d) Slip distribution estimated as Gaussian functions along each downdip profile (model iii). (e) Slip modelled as a tapered rectangular function (model iv). (f) Slip modelled as a single 2-D Gaussian function on the thrust interface (model v). In panels (g) and (h) site CH15 has been eliminated, and slip distributions estimated for independent nodes (as in a and b); and as a single 2-D Gaussian function (as in f), respectively. The colour scale indicates the magnitude of slip on the plate interface. Black arrows show residual displacements (model subtracted from observations; observations and model vectors are shown in Fig. S4). Black dots show the location of nodes in the models. Grey lines show depth contours to the plate interface (Hayes *et al.* 2012); contours are labelled in (a) in km. Black star shows the USGS epicentre of the earthquake. The maximum slip (Sx), moment magnitude (M_w), and χ^2 are given for each model.

to estimate viscosities that may be as low as 10^{18}–10^{19} Pa s and 10^{19}–10^{20} Pa s for the lower crust and upper mantle, respectively. If we assume the lower bounds of the viscosity parameters from Norabuena *et al.* (2004), the viscoelastic response could account for ∼25 per cent of the observed post-seismic deformation (Fig. 7). We thus conclude that viscoelastic relaxation is not the dominant process for the observed post-seismic deformation following the 2012 El Salvador earthquake. We assume in the following section that the post-seismic deformation is solely caused by afterslip, but discuss later the effects that viscoelastic relaxation may have on our interpretation.

To estimate the magnitude and spatial variation in the afterslip distribution, we inverted cumulative post-seismic displacements from sites in El Salvador (AIES, SSIA, SNJE, and VMIG) and Nicaragua (CHIN, CN22, LEME and TELN) from 100, 200, 300, 400 and 500 d following the 2012 El Salvador earthquake (Fig. 5; Table S1) using TDEFNODE with the same plate interface geometry as described above. The limited spatial distribution of available

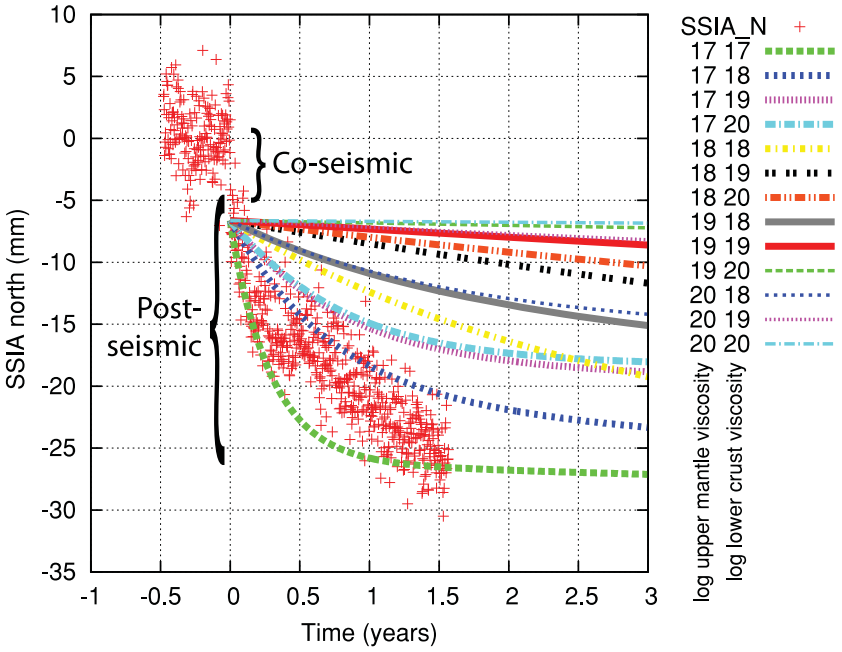

Figure 7. Results of viscoelastic modelling for the north component of station SSIA for a range of upper mantle and lower crust viscosities. The time-series data for SSIA were corrected for linear, annual and semi-annual motion (see Fig. 4).

stations (Fig. 5) offers only employment of the very simplest slip distribution models. Thus we only modelled the slip distribution as a single 2-D Gaussian function on the subduction interface [same as coseismic model (v) above; Fig. 6f].

The best-fitting slip distributions for the cumulative post-seismic displacements (Fig. 8) indicate that slip was focused near the epicentral area during the first 100 d, then progressed further downdip (maximum slip at ∼50 km depth) for the remainder of the transient period. The cumulative moment we estimate from these post-seismic slip models increases from 2.8×10^{19} to 3.2×10^{20} Nm (M_w6.9 to M_w7.6) during the first 100–500 d, respectively (Fig. 8; Table S9). To test if post-seismic deformation from the Nicoya earthquake affects our results, we also ran models excluding sites CN22, LEME and TELN. These models show comparable results to the models where those sites are included (Fig. S6). Therefore, our results are not sensitive to post-seismic deformation of the Nicoya earthquake.

The post-seismic deformation can also be fit with afterslip at shallower depths, allowing for estimates of the possible range in moment release. When maximum slip is forced to be at 25–30 km depth the cumulative moment release is predicted to increase from 2.2×10^{19} to 1.1×10^{20} Nm (M_w6.8 to M_w7.3) during the first 100 d versus 500 d, respectively. This model (with maximum slip at 25–30 km) gives a lower bound for the total post-seismic moment release, assuming that no viscoelastic deformation occurred. However, if the afterslip is located at even shallower depths (<5 km), then the post-seismic moment release needs to be higher, 6.0×10^{20} Nm (M_w7.8) for the first 500 d, to match the displacements. This result, therefore, gives an upper bound for the total post-seismic moment release. For comparison, we estimate a coseismic moment of 7.7×10^{19}–1.4×10^{20} Nm.

In the case that viscous relaxation plays an important role, the main effect is that the total moment we estimate for the afterslip would be less. If we assume that 25 per cent of the observed post-seismic signal is caused by viscous relaxation, as indicated by the preferred rheological model of Norabuena *et al.* (2004), then the afterslip, and hence geodetic moments we estimate for the afterslip above would be 25 per cent less.

4 DISCUSSION

The 2012 August 27 El Salvador earthquake is an important event because it is the largest megathrust earthquake that has occurred on this segment of the Middle America subduction interface in instrumented times (Ambraseys & Adams 1996; Fernández *et al.* 2004) and was a tsunami earthquake (Ye *et al.* 2013). Below we discuss slip localization in relation to aftershock locations, large post-seismic deformation at other margins and tectonic settings, and how interseismic strain may accumulate offshore El Salvador.

4.1 Co- and post-seismic slip localization

The estimated centroid of our coseismic slip distribution coincides with the seismically derived hypocentre (Fig. 6), indicating good agreement between seismic and geodetic solutions. However, the location and amplitude of the post-seismic slip distribution are more poorly constrained than for the coseismic deformation, because of the fewer number of stations. Aftershock locations often correlate with the location of afterslip (e.g. Lange *et al.* 2014), and here we consider the relation of aftershocks and afterslip offshore El Salvador and Nicaragua. In order to define what are aftershocks versus the background rate of seismicity, it is important to consider what the rate of previous seismicity was for the same fault segment. We compared seismicity observed by the national seismic networks in El Salvador and Nicaragua, from two equally long time periods, 2010 October 25 to 2012 August 26 and 2012 August 27 to 2014 June 30 (Fig. 9). We considered only earthquakes of magnitude 3 or greater and removed upper-crustal earthquakes along the CAFA–Caribbean boundary. There is a marked increase in seismicity in the epicentral region and to the west and northwest of the epicentre (box 1 in Fig. 9), in the same region where we observe maximum

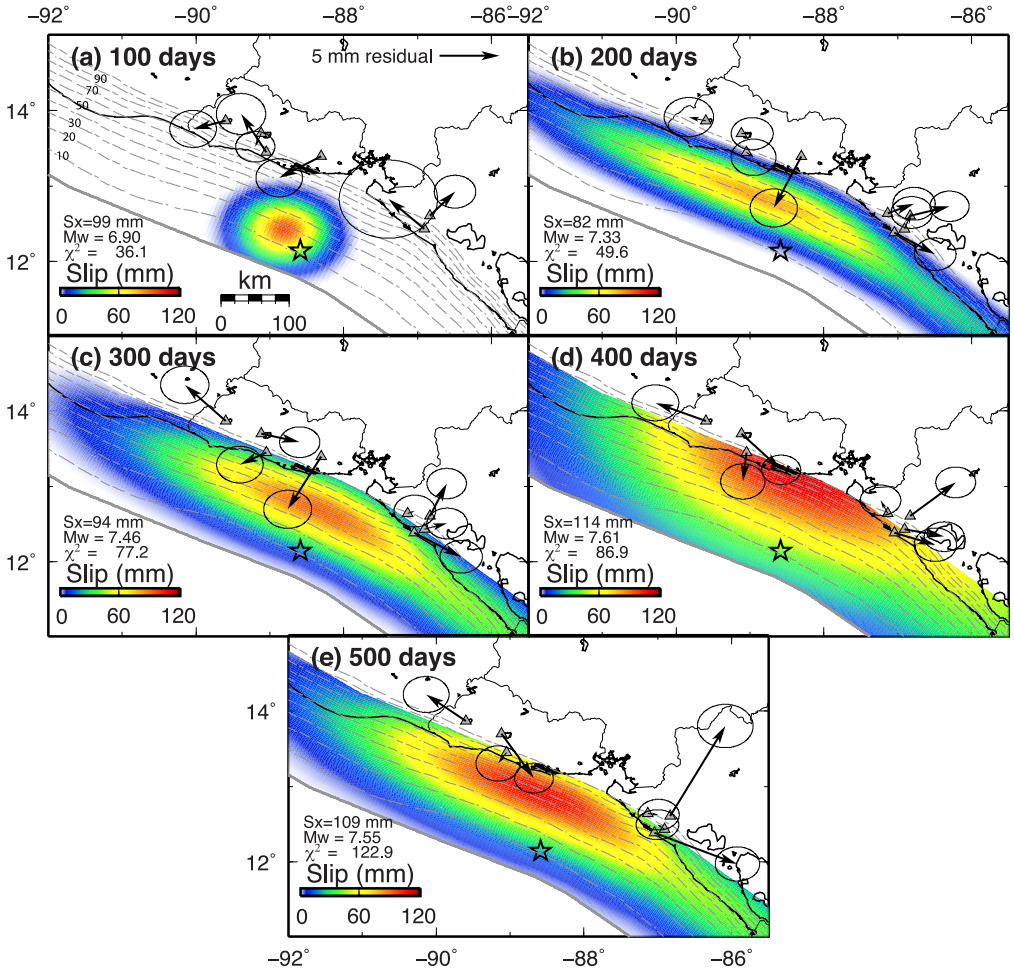

Figure 8. Surface projection of estimated cumulative post-seismic slip distribution after 100, 200, 300, 400 and 500 d after the main shock (a–e, respectively). The colour scale indicates the amount of slip on the plate interface. Residual displacements are shown as black vectors; black star shows the USGS epicentre of the earthquake. Grey lines show depth contours to the plate interface (Hayes *et al.* 2012); contours are labelled in (a) in km. The maximum slip (Sx), moment magnitude (M_w), and χ^2 are given for each model.

slip in the first 100 d following the earthquake (Fig. 8a). The aftershock activity in the epicentral area decays rapidly during the first few months after the El Salvador earthquake, but stays above pre-2012 levels into 2014 (Fig. 9c). The colocation of the aftershocks and estimated afterslip centroid strongly suggests that during the first 3 months the afterslip was indeed occurring in the epicentral area.

The depths we estimate for the cumulative afterslip at 200 d and later following the earthquake are downdip of the epicentre (Figs 8b–e). Although this depth corresponds to a band of persistent seismicity (boxes 2 and 3 in Fig. 9), there is no obvious change in the seismicity rate in this area until March 2014 (Figs 9d and e). A magnitude 6.5 earthquake with a thrust focal mechanism occurred offshore Nicaragua on 2013 June 15 (Fig. S8; Box 4 in Fig. 9b) at 40 km depth. This earthquake occurred 292 d after the 2012 August 27 El Salvador earthquake and thus does not affect our post-seismic displacement estimates at 200 d after the El Salvador earthquake. We observe ∼2 mm of coseismic displacement at LEME and CN22 from the June 2013 earthquake (Fig. S7). In March 2014 an earthquake swarm occurred offshore the Cosiguina peninsula in western Nicaragua including a magnitude 6.2 earthquake with a thrust focal mechanism at 60 km depth on 2014 March 2, 583 d after the 2012 August 27, earthquake (Figs 9b and e; Fig. S7).

The extent of the observed post-seismic deformation and aftershocks indicates that slip, mostly aseismic, but also including several $M > 6$ earthquakes, was triggered on a ∼150–200-km-long section of the megathrust offshore El Salvador and western Nicaragua by the 2012 August 27 El Salvador earthquake. In our interpretation, these observations of seismic and aseismic slip following the 2012 August 27 earthquake signify weak coupling and conditionally stable friction on the subduction interface offshore El Salvador and Nicaragua.

4.2 Relative magnitude of co- and post-seismic deformation

The moment released post-seismically over months or years following an earthquake is usually less than a third of the near-instantaneous coseismic moment release (e.g. Lin *et al.* 2013). For the 2012 August 27, El Salvador earthquake we estimate that the post-seismic moment release after 500 d was one to eight times that of the coseismic. Large post-seismic deformation was also observed for the 2004 October 9, M_w6.9 Nicaragua earthquake (Fig. 1), located about 250 km southeast of the 2012 El Salvador earthquake at cGPS station MANA, where post-seismic displacements exceeded coseismic by a factor of 2 (Fig. S8). This indicates that the Central

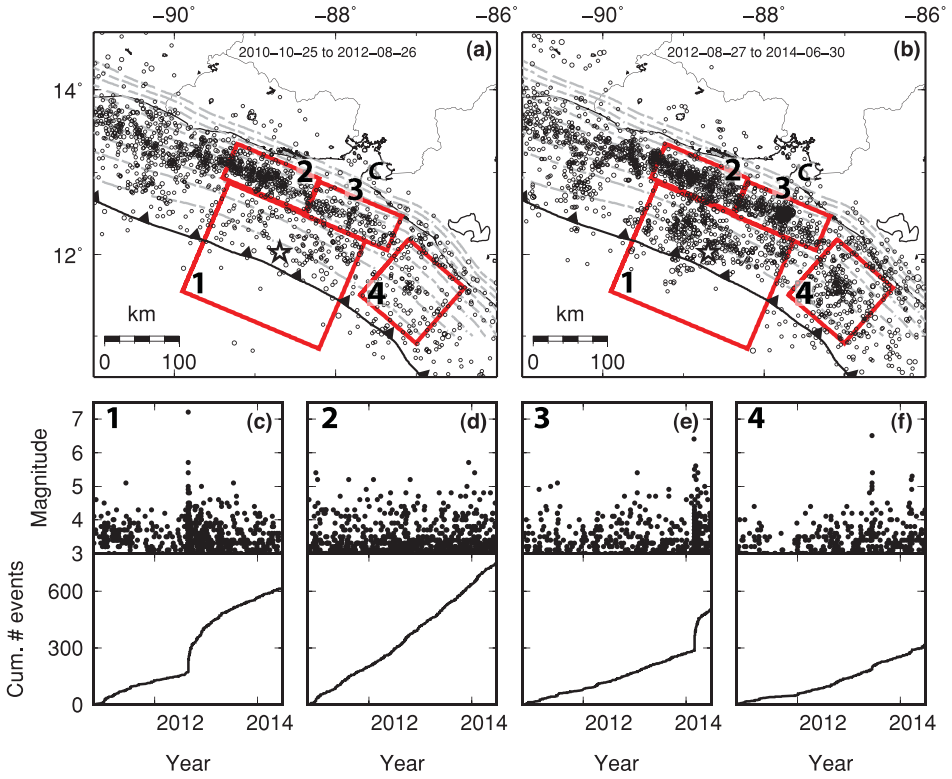

Figure 9. Earthquake activity offshore El Salvador and Nicaragua during 2010–2014. Panels (a) and (b) show earthquake locations of $M > 3$ earthquakes from the seismic networks in El Salvador (SNET) and Nicaragua (INETER) for equally long time periods before and after the 2012 August 27, El Salvador earthquake. Upper crustal earthquakes along the forearc-Caribbean Plate boundary in El Salvador and Nicaragua have been removed from the data set. Star shows SNET's location of the 2012 August 27 earthquake. Dashed grey lines show 10 km depth contours of the plate interface as defined by Hayes *et al.* (2012). Earthquake magnitude and cumulative number of earthquakes for data within boxes 1–4 in (a) and (b) are shown in (c) to (f). C, Cosiguina Peninsula.

America margin offshore El Salvador and Nicaragua has similar properties that allow for excessive post-seismic deformation. Elsewhere along the Middle America trench, post-seismic afterslip triggered by the 2012 March 20 M_w7.5 Ometepec, southern Mexico earthquake, equalled 140 per cent of the coseismic moment by 6 months after the earthquake and affected an area of the subduction interface ∼10 times larger than the coseismic slip (Graham *et al.* 2014).

Large post-seismic deformation has also been observed at other subduction zones. In Indonesia, Feng *et al.* (2011) note rapid afterslip following the 2010 M_w7.8 Mentawai earthquake, where post-seismic displacements nearly equal the coseismic displacements after 8 months. At the Japan subduction zone, Suito *et al.* (2011) observed a high ratio of post-seismic to coseismic displacements following three earthquakes that occurred in the source region of the 2011 Tohoku earthquake in 2005, 2008 and 2010 of magnitudes 7.2, 6.9 and 6.7, respectively. The ratios of the post- to coseismic moments for these events, based on geodetic inversions, are 1.8, 3.6 and 3.1, respectively. The 2005 event occurred in a region where strong coupling has been estimated (>80 per cent), whereas the 2008 and 2010 earthquakes occurred in less coupled areas (∼50 per cent; Suwa *et al.* 2006; Loveless and Meade 2011). These events thus indicate that large post-seismic deformation compared to coseismic deformation is not a unique characteristic of weakly coupled margins, but may also be characteristic of areas that straddle the transition from strong interseismic locking to aseismic creep. An alternative explanation of large post-seismic deformation lies in the geometry of the subduction zone. Slip on the shallowest (<5–10 km depth) parts of the subduction zone is poorly expressed in deformation on land, while slip at greater depths is more effectively translated to geodetic sites measuring surface deformation (Fig. S2). Therefore, if the coseismic slip is at shallow depths and the post-seismic slip is further downdip, the post-seismic slip results in relatively greater measured surface deformation compared to the moment released.

Following the 2004 *M*6 Parkfield strike-slip earthquake, the moment released as afterslip was found to be at least three times larger than the coseismic moment (Freed 2007; Barbot *et al.* 2009). The post-seismic moment at Parkfield was released as low magnitude slip (less than the coseismic slip) over a large segment of the fault, compared to the patch that failed coseismically. Parkfield is in the boundary region between the creeping and non-creeping sections of the San Andreas fault (Murray & Langbein 2006), with intermediate locking, analogous to the seismogenic- to freely slipping transition on a megathrust. The relatively large post-seismic deformation observed for the El Salvador earthquake thus suggests that on this segment of the Middle America margin, velocity-weakening patches that slip coseismically are bridged by large areas of velocity-strengthening or conditionally stable areas that constitute the regions of afterslip.

4.3 Strain accumulation and release

Strain accumulation and release over the earthquake cycle depends on the frictional characteristics of the plate interface, and elastic and viscous properties of the converging plates. Sediment input, fluid pressure, temperature, roughness and faulting of the subducting plate affect the frictional properties of the plate interface (e.g.

Wallace *et al.* 2009; Wang and Bilek 2011 and references therein). Large release of moment as aseismic after-slip as compared to coseismic slip indicates large patches of stable or conditionally stable frictional characteristics. Evidently earthquakes do occur at the El Salvador margin indicating strain accumulation on velocity-weakening patches. It has been proposed that tsunami earthquakes are manifestations of frictional conditional stability (Bilek and Lay 2002). Although Byrne *et al.* (1988) suggested that strain is not accumulated at the shallowest portions of subduction zones, sediment-starved subduction zones have been suggested to be capable of accumulating strain at shallow depths (Polet & Kanamori 2000). Gagnon *et al.* (2005) used seafloor-geodetic observations offshore Peru, a sediment-starved margin, to verify that the subduction zone in that location was not slipping (i.e. strongly coupled) up to at least 2 km depth during the interseismic period. The 2012 El Salvador earthquake occurred in a sediment-starved region where the subducting crust is also heavily faulted (Fig. 1), both of which have been proposed as important factors for facilitating tsunami earthquakes (Polet & Kanamori 2000).

We estimate a maximum coseismic slip between 0.2 and 5 m, for the 2012 El Salvador earthquake, based on the inversion of our geodetic data and choice of model constraints (Fig. 6), while Ye *et al.* (2013) estimate approximately 1 m of maximum slip and long duration for the earthquake. If we assume full coupling on the patch that failed coseismically and that the last earthquake did occur in 1919, using the Cocos–CAFA relative convergence rate of 76 mm yr^{-1} (Kobayashi *et al.* 2014), there should have been ∼7 m of accumulated slip deficit. This is significantly greater than the maximum slip estimates, suggesting that significant strain is released aseismically along the margin, potentially as slow-slip events or that strain is accumulated at less than 100 per cent because of the weak nature of the margin (Correa-Mora *et al.* 2009; LaFemina *et al.* 2009; Kobayashi *et al.* 2014).

Afterslip contributes significantly to the total moment budget on the subduction interface, but likely the afterslip is manifested as low slip over a large area. If the frictional and mechanical characteristics that facilitate tsunami earthquakes are the same for regions of afterslip, we can speculate that relatively large post-seismic deformation should in general follow tsunami earthquakes. We suggest that the best way forward to address shallow strain accumulation along convergent margins is through repeated seafloor-geodetic observations.

5 CONCLUSIONS

We find that the M_w 7.3 2012 August 27 El Salvador tsunami earthquake occurred on shallow parts of the plate interface and was followed by significant afterslip, causing the observed post-seismic deformation to exceed the coseismic deformation in less than 1 yr. The high ratio of post- to coseismic deformation does not necessarily translate into a high ratio of co- and post-seismic moment (we estimate M_w 7.2–7.8 for the afterslip), but depends also on how deep on the fault the afterslip occurs compared to the coseismic slip.

ACKNOWLEDGEMENTS

We thank everyone contributing to collection of episodic and continuous GPS data in the study area. We thank INETER, Nicaragua, for field support. SNET, El Salvador and INETER, Nicaragua, provided earthquake data for the study. Figures were prepared using the GMT software (Wessel & Smith 1998). This manuscript benefited from insightful comments from Editor Duncan Agnew and reviewers Laura Wallace and Andreas Hoechner. This study was supported by a UNAVCO COCONet fellowship to HG and by a National Science Foundation grant (EAR-0911546) to PL. This material is based on services provided by the UNAVCO Facility with support from NSF and the National Aeronautics and Space Administration (NASA) under NSF Cooperative Agreement No. EAR-0735156.

REFERENCES

Ambraseys, N. & Adams, R., 1996. Large-magnitude central American earthquakes, 1898–1994, *Geophys. J. Int.,* **127,** 665–692.

Barbot, S. & Fialko, Y., 2010. A unified continuum representation of post-seismic relaxation mechanisms: semi-analytic models of afterslip, poroelastic rebound and viscoelastic flow, *Geophys. J. Int.,* **182**(3), 1124–1140.

Barbot, S., Fialko, Y. & Bock, Y., 2009. Postseismic deformation due to the M_w6.0 2004 Parkfield earthquake: stress driven creep on a fault with spatially variable rate-and-state friction parameters, *J. geophys. Res.,* **114,** B07405, doi:10.1029/2008JB005748.

Bilek, S.L. & Lay, T., 2002. Tsunami earthquakes possibly widespread manifestations of frictional conditional stability, *Geophys. Res. Lett.,* **29**(14), doi:10.1029/2002GL015215.

Blewitt, G., 2008. Fixed point theorems of GPS carrier phase ambiguity resolution and their application to massive network processing: Ambizap, *J. geophys. Res.,* **113,** B12410, doi:10.1029/2008JB005736.

Bommer, J. *et al.*, 2002. The El Salvador earthquakes of January and February 2001: context, characteristics and implications for seismic risk, *Soil Dyn. Earthq. Eng.,* **22**(5), 389–418.

Byrne, D.E., Davis, D.M. & Sykes, L.R., 1988. Loci and maximum size of thrust earthquakes and the mechanics of the shallow region of subduction zones, *Tectonics,* **7**(4), 833–857.

Correa-Mora, F. *et al.*, 2009. GPS-derived coupling estimates for the Central America subduction zone and volcanic arc faults: El Salvador, Honduras and Nicaragua, *Geophys. J. Int.,* **179**(3), 1279–1291.

DeMets, C., 2001. A new estimate for present-day Cocos-Caribbean Plate motion: implications for slip along the Central American Volcanic Arc, *Geophys. Res. Lett.,* **28**(21), 4043–4046.

DeMets, C., Gordon, R. & Argus, D., 2010. Geologically current plate motions, *Geophys. J. Int.,* **181,** 1–80.

Dewey, J.W., White, R.A. & Hernandez, D.A., 2004. Seismicity and tectonics of El Salvador, *Spec. Papers—Geol. Soc. Am.,* **375,** 363–378.

Ellis, A.P. *et al.*, 2015. Geodetic slip solutions for the M_w = 7.4 Champerico (Guatemala) earthquake of 2012 November 7 and its postseismic deformation, *Geophys. J. Int.,* **201**(2), 856–868.

Feng, L., Hill, E.M., Banerjee, P., Lubis, A.M., Qiu, Q. & Sieh, K.E., 2011. Very rapid afterslip following the shallow 2010 M_w7.8 Mentawai tsunami earthquake, in *Abstract T23C-2405 presented at 2011 Fall Meeting,* AGU, San Francisco, CA, 5–9 December.

Fernández, M., Ortiz-Figueroa, M. & Mora, R., 2004. Tsunami hazards in El Salvador, *Spec. Paper—Geol. Soc. Am.,* **375,** 435–444.

Freed, A.M., 2007. Afterslip (and only afterslip) following the 2004 Parkfield, California, earthquake, *Geophys. Res. Lett.,* **34,** L06312, doi:10.1029/2006GL029155.

Gagnon, K., Chadwell, C.D. & Norabuena, E., 2005. Measuring the onset of locking in the Peru-Chile trench with GPS and acoustic measurements, *Nature,* **434,** 205–208.

Geirsson, H. *et al.*, 2014. Multidisciplinary observations of the 2011 explosive eruption of Telica volcano, Nicaragua: implications for the dynamics of low-explosivity ash eruptions, *J. Volc. Geotherm. Res.,* **271,** 55–69.

Graham, S.E., DeMets, C., DeShon, H.R., Rogers, R., Maradiaga, M.R., Strauch, W., Wiese, K. & Hernandez, D., 2012. GPS and seismic constraints on the M = 7.3 2009 Swan Islands earthquake: implications for stress changes along the Motagua fault and other nearby faults, *Geophys. J. Int.,* **190**(3), 1625–1639.

Graham, S.E. *et al.*, 2014. GPS constraints on the M_w = 7.5 Ometepec earthquake sequence, southern Mexico: coseismic and post-seismic deformation, *Geophys. J. Int.,* **199**(1), 200–218.

Hayes, G.P., 2012. Finite fault model for the Sep 5, 2012 M_w7.6 Costa Rica Earthquake, Available at: http://earthquake.usgs.gov/earthquakes/eqinthenews/2012/usc000cfsd/finite_fault.php, last accessed 17 October 2012.

Hayes, G.P., Wald, D.J. & Johnson, R.L., 2012. Slab1.0: a three-dimensional model of global subduction zone geometries, *J. geophys. Res.,* **117,** B01302, doi:10.1029/2011JB008524.

Hill, E.M. *et al.*, 2012. The 2010 M_w7.8 Mentawai earthquake: very shallow source of a rare tsunami earthquake determined from tsunami field survey and near-field GPS data, *J. geophys. Res.,* **117**(B6), B06402, doi:10.1029/2012JB009159.

Kanamori, H., 1972. Mechanism of tsunami earthquakes, *Phys. Earth planet. Inter.,* **6,** 346–359.

Kanamori, H., 2014. The dirversity of large earthquakes and its implications for hazard mitigation, *Annu. Rev. Earth planet. Sci.,* **42,** 7–26.

Kanamori, H. & Kikuchi, M., 1993. The 1992 Nicaragua earthquake: a slow tsunami earthquake associated with subducted sediments, *Nature,* **361,** 714–716.

Kobayashi, D., LaFemina, P., Geirsson, H., Chichaco, E., Abrego, A.A., Mora, H. & Camacho, E., 2014. Kinematics of the western Caribbean: collision of the Cocos Ridge and upper plate deformation, *Geochem. Geophys. Geosyst.,* **15,** 1671–1683.

LaFemina, P. *et al.*, 2009. Fore-arc motion and Cocos Ridge collision in Central America, *Geochem. Geophys. Geosyst.,* **10**(5), Q05S14, doi:10.1029/2008GC002181.

Lange, D., Bedford, J., Moreno, M., Tilmann, F., Baez, J.C., Bevis, M. & Kruger, F., 2014. Comparison of postseismic afterslip models with aftershock seismicity for three subduction-zone earthquakes: Nias 2005, Maule 2010 and Tohoku 2011, *Geophys. J. Int.,* **199**(2), 784–799.

Lin, Y.N.N. *et al.*, 2013. Coseismic and postseismic slip associated with the 2010 Maule Earthquake, Chile: characterizing the Arauco Peninsula barrier effect, *J. geophys. Res. Solid Earth,* **118**(6), 3142–3159.

Loveless, J.P. & Meade, B.J., 2011. Spatial correlation of interseismic coupling and coseismic rupture extent of the 2011 M W = 9.0 Tohoku-oki earthquake, *Geophys. Res. Lett.,* **38,** L17306, doi:10.1029/2011GL048561.

Martínez-Díaz, J.J., Álvarez-Gómez, J.A., Benito, B. & Hernández, D., 2004. Triggering of destructive earthquakes in El Salvador, *Geology,* **32**(1), 65–68.

McCaffrey, R., 2009. Time-dependent inversion of three-component continuous GPS for steady and transient sources in northern Cascadia, *Geophys. Res. Lett.,* **36,** L07304, doi:10.1029/2008GL036784.

Murray, J. & Langbein, J., 2006. Slip on the San Andreas fault at Parkfield, California, over two earthquake cycles, and the implications for seismic hazard, *Bull. seism. Soc. Am.,* **96,** S283–S303.

Norabuena, E. *et al.*, 2004. Geodetic and seismic constraints on some seismogenic zone processes in Costa Rica, *J. geophys. Res.,* **109,** B11403, doi:10.1029/2003JB002931.

Polet, J. & Kanamori, H., 2000. Shallow subduction zone earthquakes and their tsunamigenic potential, *Geophys. J. Int.,* **142,** 684–702.

Protti, M. *et al.*, 2013. Nicoya earthquake rupture anticipated by geodetic measurement of the locked plate interface, *Nat. Geosci.,* **7**(2), 117–121.

Satake, K. & Tanioka, Y., 1999. Sources of Tsunami and tsunamigenic earthquakes in subduction zones, *Pure appl. Geophys.,* **154**(3-4), 467–483.

Suito, H., Nishimura, T., Tobita, M., Imakiire, T. & Ozawa, S., 2011. Interplate fault slip along the Japan Trench before the occurrence of the 2011 off the Pacific coast of Tohoku Earthquake as inferred from GPS data, *Earth, Planets Space,* **63**(7), 615–619.

Suwa, Y., Miura, S., Hasegawa, A., Sato, T. & Tachibana, K., 2006. Interplate coupling beneath NE Japan inferred from three-dimensional displacement field, *J. geophys. Res.,* **111,** B04402, doi:10.1029/2004JB003203.

Turner, H., LaFemina, P., Saballos, A., Mattioli, G.S., Jansma, P. & Dixon, T., 2007. Kinematics of the Nicaraguan forearc from GPS geodesy, *Geophys. Res. Lett.,* **34,** L02302, doi:10.1029/2006GL027586.

Valleé, M., Bouchon, M. & Schwartz, S.Y., 2003. The 13 January 2001 El Salvador earthquake: a multidata analysis, *J. geophys. Res.,* **108**(B4), 2203, doi:10.1029/2002JB001922.

Wallace, L.M. *et al.*, 2009. Characterizing the seismogenic zone of a major plate boundary subduction thrust: Hikurangi Margin, New Zealand, *Geochem., Geophys. Geosyst.,* **10**(10), Q10006, doi:10.1029/2009GC002610.

Wang, K. & Bilek, S.L., 2011. Do subducting seamounts generate or stop large earthquakes?, *Geology,* **39**(9), 819–822.

Wdowinski, S., Bock, Y., Zhang, J., Fang, P. & Genrich, J., 1997. Southern California permanent GPS geodetic array: spatial filtering of daily positions for estimating coseismic and postseismic displacements induced by the 1992 Landers earthquake, *J. geophys. Res.,* **102**(B8), 18 057–18 070.

Wessel, P. & Smith, H.F., 1998. New improved version of the generic mapping tools released, *EOS, Trans. Am. Geophys. Un.,* **79,** 579, doi:10.1029/98EO00426.

White, R.A., Ligorría, J.P. & Cifuentes, I.L., 2004. Seismic history of the Middle America subduction zone along El Salvador, Guatemala, and Chiapas, Mexico: 1526–2000, *Spec. Papers—Geol. Soc. Am.,* **375,** 379–396.

Ye, L., Lay, T. & Kanamori, H., 2013. Large earthquake rupture process variations on the Middle America megathrust, *Earth planet. Sci. Lett.,* **381,** 147–155.

Zumberge, J., Heflin, M., Jefferson, D., Watkins, M. & Webb, F., 1997. Precise Point Positioning for the efficient and robust analysis of GPS data from large networks, *J. geophys. Res.,* **102,** 5005–5017.

SUPPORTING INFORMATION

Additional Supporting Information may be found in the online version of this paper:

Figure S1. Kinematic analysis of 30-s GPS data from stations AIES, VMIG and SSIA. The origin time of the earthquake is indicated with a vertical dashed line. The data were processed using the GIPSY/ASIS II software in precise-point-positioning mode for kinematic data using loose constraints on the solutions. The coseismic offsets in the north component based on 24-hr solutions are −0.7, −1.2 and −1.1 cm for SSIA, VMIG and AIES, respectively (Table 1), which is in agreement with the epoch-by-epoch solution displayed here.

Figure S2. Displacements from four different sections of the thrust interface as a function of distance from the trench. We only display the results from the coastline inland. (a) Dashed line shows the plate interface from the Slab 1.0 model of Hayes et al. (2012), and coloured dashes mark the location of each of the sections we calculate displacement for. Each section is 10 km long along-dip and 150 km along-strike. The segments are at 0, 30, 60 and 90 km distance from the trench, corresponding to top depths of 0, 8, 19 and 46 km, respectively, following the slab geometry of Hayes et al. (2012). (b) Horizontal, and c) vertical deformation. Different slip of uniform amplitude is applied to each section (8, 1, 0.4 and 0.5 m for sections 1, 2, 3 and 4, respectively) to generate a similar horizontal displacement on land. Larger slip is needed on shallow sections of the thrust interface compared to deeper sections to generate similar displacements.

Figure S3. Checkerboard resolution tests. Panels (a) and (c) show synthetic slip distributions for 8 × 8 and 6 × 6 nodes of uniform slip, respectively. Panels (b) and (d) show the recovered slip distribution. Slip of 0.1 m is applied to the slipping patches and the deformation is calculated at all stations used in the coseismic inversion. The 0.1 m of slip gives deformation on the same order of magnitude as for our coseismic deformation at the station locations. In the inverse model we start with zero slip on all nodes and invert the signal calculated from the forward model, using model setup 'i' (see Section 3.1). The colour scale is chosen such that no colour (white) is applied

where slip is less than 1 per cent of the maximum slip on the scale. Smaller checkers then shown here (i.e. 4 × 4 nodes and below) are poorly recovered.

Figure S4. As Fig. 6, except instead of the residual vector we show the modelled and observed displacements at our sites.

Figure S5. Residual displacements from the slip distribution of Ye *et al.* (2013).

Figure S6. Surface projection of estimates of cumulative post-seismic slip distribution after 100, 200, 300, 400 and 500 d after the main shock (a–e, respectively). Sites CN22, LEME, and TELN are not included in the inversion. The colour scale indicates the amount of slip on the plate interface, and is different from what shown in Fig. 8. Black arrows show residual displacements. Black star shows the epicentre of the earthquake according to USGS. The maximum slip (Sx), resulting moment magnitude (M_w), and χ^2 are given for each model.

Figure S7. Coseismic deformation from the 2013 June 15, M_w = 6.5 earthquake offshore Nicaragua, location from INETER shown with a star. Red arrows show predicted displacements based on the GCMT moment tensor (M_w = 6.5; strike 303°; dip 33°, rake 89°) and INETER location and depth (40 km). Black arrows show displacements estimated from cGPS time-series with 1σ uncertainties. Grey circles show location of M > 3 earthquakes from 2012 August 27, to 2014 June 30, from the Nicaraguan seismic network. Upper crustal earthquakes at the CAFA–Caribbean Plate boundary have been removed from the seismic catalogue.

Figure S8. Time-series for east and north components of station MANA in Nicaragua. The time-series were detrended using the mean velocity during 2008.0 to 2012.6. Vertical dashed lines mark the times of the M_w6.9 2004 October 9 Nicaragua and M_w7.3 2012 August 27 El Salvador and Nicoya earthquakes. For the 2004 earthquake the coseismic deformation is −5 and −10 mm in east and north components, respectively, while the post-seismic deformation is −3 and −22 mm, respectively.

Table S1. Cumulative post-seismic deformation at GPS stations.

Table S2. Predicted co-seismic displacements for the 2012 August 27 El Salvador earthquake, based on the best-fitting model, on a grid of 0.2 × 0.2 degrees.

Table S3. Predicted co-seismic displacements for the 2012 August 27 El Salvador earthquake, based on the best-fitting model, at GPS station locations.

Table S4. Slip distribution for best-fitting model of coseismic deformation. Format follows TDEFNODE conventions for .nod files (see TDEFNODE manual).

Table S5. Slip distribution for best-fitting model of cumulative post-seismic deformation for the first 100 d. Format follows TDEFNODE conventions for .nod files (see TDEFNODE manual).

Table S6. Slip distribution for best-fitting model of cumulative post-seismic deformation for the first 200 d. Format follows TDEFNODE conventions for .nod files (see TDEFNODE manual).

Table S7. Slip distribution for best-fitting model of cumulative post-seismic deformation for the first 300 d. Format follows TDEFNODE conventions for .nod files (see TDEFNODE manual).

Table S8. Slip distribution for best-fitting model of cumulative post-seismic deformation for the first 400 d. Format follows TDEFNODE conventions for .nod files (see TDEFNODE manual).

Table S9. Slip distribution for best-fitting model of cumulative post-seismic deformation for the first 500 d. Format follows TDEFNODE conventions for .nod files (see TDEFNODE manual).

Table S10. Predicted cumulative displacements after 500 d from the 2012 August 27 El Salvador earthquake.

(http://gji.oxfordjournals.org/lookup/suppl/doi:10.1093/gji/ggv244/-/DC1).

Please note: Oxford University Press is not responsible for the content or functionality of any supporting materials supplied by the authors. Any queries (other than missing material) should be directed to the corresponding author for the paper.